University of Pennsylvania
ScholarlyCommons

Departmental Papers (CBE)

Department of Chemical & Biomolecular Engineering

7-15-2003

Internally Consistent Approach for Modeling Solid-State Aggregation: I. Atomistic Calculations of Vacancy Clustering in Silicon

Manish Prasad
University of Pennsylvania

Talid R. Sinno
University of Pennsylvania, talid@seas.upenn.edu

Postprint version. Published in *Physical Review B* Volume 68, Number 4, (2003) 45206 1-12. Publisher URL: http://dx.doi.org/10.1103/PhysRevB.68.045206

This paper is posted at ScholarlyCommons. http://repository.upenn.edu/cbe_papers/4
For more information, please contact repository@pobox.upenn.edu.

Internally Consistent Approach for Modeling Solid-State Aggregation: I. Atomistic Calculations of Vacancy Clustering in Silicon

Abstract

A computational framework is presented for describing the nucleation and growth of vacancy clusters in crystalline silicon. The overall approach is based on a parametrically consistent comparison between two representations of the process in order to provide a systematic method for probing the details of atomic mechanisms responsible for aggregation. In this paper, the atomistic component of the overall framework is presented. First, a detailed set of targeted atomistic simulations are described that characterize fully the thermodynamic and transport properties of vacancy clusters over a wide range of sizes. It is shown that cluster diffusion is surprisingly favorable because of the availability of multiple, almost degenerate, configurations. A single large-scale parallel molecular dynamics simulation is then used to compute directly the evolution of the vacancy cluster size distribution in a supersaturated system initially containing 1000 uniformly distributed vacancies in a host lattice of 216,000 Si atoms at 1600 K. The results of this simulation are interpreted in the context of mean-field scaling theory based on the observed power-law evolution of the size distribution moments. It is shown that the molecular dynamics results for aggregation of vacancy clusters, particularly the evolution of the average cluster size, can be very well represented by a highly simplified mean-field model. A direct comparison to a detailed continuum model is made in a subsequent article.

Keywords

aggregation, nucleation, silicon, vacancy clusters, molecular dynamics, simulations

Comments

Postprint version. Published in *Physical Review B* Volume 68, Number 4, (2003) 45206 1-12. Publisher URL: http://dx.doi.org/10.1103/PhysRevB.68.045206

This journal article is available at ScholarlyCommons: http://repository.upenn.edu/cbe_papers/4

An Internally Consistent Approach for Modeling Solid-State Aggregation: I. Atomistic Calculations of Vacancy Clustering in Silicon

Manish Prasad and Talid Sinno[1]
Department of Chemical Engineering
University of Pennsylvania
Philadelphia, PA 19104-6393

Received:

ABSTRACT

A computational framework is presented for describing the nucleation and growth of vacancy clusters in crystalline silicon. The overall approach is based on a parametrically consistent comparison between two representations of the process in order to provide a systematic method for probing the details of atomic mechanisms responsible for aggregation. In this paper, the atomistic component of the overall framework is presented. First, a detailed set of targeted atomistic simulations are described that characterize fully the thermodynamic and transport properties of vacancy clusters over a wide range of sizes. It is shown that cluster diffusion is surprisingly favorable because of the availability of multiple, almost degenerate, configurations. A single large-scale parallel molecular dynamics simulation is then used to compute directly the evolution of the vacancy cluster size distribution in a supersaturated system initially containing 1000 uniformly distributed vacancies in a host lattice of 216,000 Si atoms at 1600 K. The results of this simulation are interpreted in the context of mean-field scaling theory based on the observed power-law evolution of the size distribution moments. It is shown that the molecular dynamics results for aggregation of vacancy clusters, particularly the evolution of the average cluster size, can be very well represented by a highly simplified mean-field model. A direct comparison to a detailed continuum model is made in a subsequent article.

PACS #: 61.72Ji

[1] Corresponding Author: talid@seas.upenn.edu

I. INTRODUCTION

The design and control of microstructural evolution is central to the processing of materials ranging from metals to plastics to ceramics. One of the most tightly controlled processes is microelectronic device fabrication on crystalline semiconductor substrates. In the case of crystalline silicon, the most common semiconductor material, nucleation and aggregation of point defects are responsible for the formation of a wide variety of defects (generally known as microdefects)[1,2]. While most microdefects are detrimental to microelectronic device function, some can be useful if their size and spatial distributions can be controlled[3]. The latter issue also is relevant for the future fabrication of nanoscale electronic devices based on quantum dots[4,5]. The most fundamental building blocks for microdefect formation in crystalline materials are native point defects, namely the self-interstitial and the vacancy. These two species are the mediators for impurity diffusion[6,7] and also lead to large clusters by aggregation[1,2,8].

While theory and simulation have played important roles in the refinement of silicon processing technology with respect to the control of point defect distributions and microdefect formation[8,9,10], most of the commercially significant progress has come about by careful experimentation[11,12,13]. In fact, process scale (continuum) modeling efforts have not yet led to robust and quantitatively predictive simulation tools. One of the principal reasons for this is the lack of reliable methods to estimate accurately the thermophysical properties of point defects and defect clusters, and therefore the precise reaction and aggregation pathways that are responsible for the observed kinetics.

There are several techniques for investigating each aspect of the overall aggregation process. At the coarsest level is the continuum approach, which reduces the description of the aggregation process to a series of coupled reaction-diffusion-advection equations. This approach is highly efficient and is not limited by maximum cluster size, but requires that all cluster physics and properties be specified *a priori*. Furthermore, all microstructural information is lost, both at the individual cluster and local distribution levels. At the other extreme is the atomic simulation approach, which considers explicitly the dynamics of each atom, but obviously cannot simulate process-relevant time and length scales. In atomistic simulation, the only required input is the interatomic potential that governs the dynamical evolution of the atomic trajectories. In between these limits are methods, such as Kinetic Monte Carlo[14,15], that attempt to retain atomistic-level detail, but coarse-grain the details of the atomic motion to allow for much larger and longer simulation scope. Once again, Kinetic Monte Carlo requires that an interaction and transport description for each cluster be specified *a priori*.

A. Internally Consistent Methodology

This paper is the first of two articles that focus on vacancy aggregation in crystalline silicon to present a multifaceted computational framework for systematically and quantitatively probing solid-state nucleation and growth phenomena. The approach is a three-pronged one: the first component consists of a series of targeted atomistic calculations, in which structural, thermodynamic, and transport data for a range of vacancy cluster sizes are computed systematically using molecular dynamics (MD) and statics (MS)[16,17]. The second component is a single large-scale parallel MD simulation in which a highly supersaturated system of vacancies is

allowed to evolve in time without any constraints. The primary result of this simulation is a transient vacancy size distribution function in a thermodynamically closed system, which is analyzed here using mean-field scaling theory. Both atomistic components employ the Environment-Dependent Interatomic Potential[18,19] (EDIP), an empirical potential that has been shown to lead to good agreement with electronic structure predictions for vacancy defect structures and energies in silicon[20].

A subsequent article will describe the third component of this study, which is a detailed, continuum-level description of the large-scale MD simulation. The continuum model is based on a mean-field approximation represented mathematically by a system of coupled Master equations[21,22]. The continuum model and the scaling analysis are parameterized entirely using atomistic simulations. The connection between these three individual components is shown schematically in Figure 1. The key result is that a *parametrically consistent*, quantitative comparison between the results of the continuum and atomistic-level models can be made, which leads to *mechanistic* (as opposed to parametric) insight into nucleation and growth phenomena.

This paper is organized as follows. Section II is a brief overview of previous modeling of vacancy clusters in silicon. Section III focuses on individual vacancy cluster structure and thermodynamics. Cluster transport properties, with emphasis on the multiple-pathway mechanism responsible for enhanced vacancy cluster diffusion, are presented in Section IV. Next, in Section V, we describe a parallel molecular dynamics simulation of vacancy aggregation in which a transient size distribution is generated. The basic features of the

aggregation process are analyzed in the context of analytical scaling theory in Section VI, which has been applied to a variety of nucleation and growth processes.

II. VACANCY AGGREGATION IN CRYSTALLINE SILICON

Vacancy aggregation in silicon has been studied extensively because large vacancy clusters (voids) are known to be harmful to microelectronic device yield and reliability, particularly gate-oxide integrity (GOI)[23,24]. Voids have been observed directly by TEM to organize into octahedral structures aligned almost exclusively along the (111) crystallographic planes of the silicon lattice[25]. This phenomenon has been explained by the low energy of the Si (111) surface relative to other orientations[26], and an important goal of this work is to make a detailed connection between the thermodynamics of small vacancy clusters and large octahedral voids.

In addition to the direct technological implications for crystal growth, the vacancy aggregation process is a prototypical model for solid-state nucleation and growth and can be used as the basis for investigation of more complex phenomena, such as coupled diffusion-aggregation problems in carbon-doped silicon[27,28]. Several investigators have developed various continuum models aimed at predicting the evolution of the void size distribution during Czochralski silicon crystal growth. These efforts (see for example, Sinno and Brown[29], Dornberger et al.[30], and Nakamura et al.[31]) have relied on the assumption of diffusion-limited homogeneous nucleation in which single vacancies attach and detach from a dynamically evolving system of clusters. While these studies have led to models that can capture the essential features of vacancy cluster formation during crystal growth, they are not yet quantitatively

predictive. It is not clear whether the reasons for this are due to an incomplete picture of the physics or whether the required thermophysical properties are insufficiently characterized.

The thermophysical properties of vacancy clusters are difficult to characterize because small clusters only can be observed indirectly (e.g. by positron annihilation and electron paramagnetic resonance)[32,33,34], and also are difficult to approach with atomistic simulation because of the large computational cells and long simulation times required for adequate relaxation. These limitations are especially significant for *ab initio* and tight-binding molecular dynamics approaches, which include the effects of electronic contributions to varying extents. Despite these limitations, notable progress in this area recently has been made. Two series of tight-binding calculations[35,36] recently have shown that the binding energies of vacancy clusters are a non-monotonic function of size, and cannot be expressed simply in terms of nearest-neighbor interactions [32,37]. In ref. [14], a second-nearest neighbor (2NN) interaction was introduced to account for vacancy cluster energetics and was found to reproduce well the tight-binding formation energies. The results in ref. [36] also were poorly represented by a simple dangling bond model, and an extended model based on new bond formation due to atomic relaxation was proposed.

The vacancy cluster formation energies computed in ref. [35] were used in Kinetic Monte Carlo (KMC) calculations to demonstrate the effect of the different binding assumptions[38]. In these KMC simulations, the results of the tight-binding estimates for cluster energies were mapped onto an Ising model (nearest neighbor interactions only) and a so-called extended Ising model (2NN interactions included). The inclusion of 2NN interactions greatly enhanced the

mobility of clusters in the KMC simulations and lead to faster-evolving, broader cluster size distributions when compared to models that only included NN interactions.

A consistent feature of all atomistic studies of vacancy clusters to date is the particular stability of certain cluster structures, namely the six-vacancy ring and the ten-vacancy adamantine cage[20,35]. The stability of the ring hexavacancy has been confirmed with *ab initio* calculations[39]. These ring and cage structures are postulated to play an important role in further cluster growth[20,35] and are further considered in Section III.

III. ATOMISTIC MODELING OF VACANCY CLUSTER THERMODYNAMICS

A detailed study of vacancy cluster thermodynamics, transport, and structure is presented based on a synergistic combination of molecular statics (MS), molecular dynamics (MD), and lattice dynamics simulations for free energy estimation. All atomistic calculations were performed with the empirical EDIP potential, which has been shown to lead to a very good representation of vacancy cluster properties. While in principle less accurate than electronic structure calculations, the use of an empirical potential allows for a wider range of phenomena to be considered dynamically, such as cluster transport and nucleation.

The dynamical simulations were used to investigate the formation and transport properties of vacancy clusters in the size range $1 \leq N \leq 30$, while the statics calculations were used to estimate the zero-temperature energies of clusters containing up to 969 vacancies embedded in host crystals containing up to 46,656 atoms. The size of the simulation cell in each case was

determined by limiting the concentration of vacancies to 2 % atomic fraction, which was found to be well below the threshold in which a cluster interacted with its periodic image. The molecular dynamics simulations were performed in the NPT ensemble using a Nose-Hoover chain method[40]. A time step of 0.23 fs was used for all simulations. Our protocol for performing the MD simulations was to carry out a set of 10 runs of 40,000 time steps at each temperature for each cluster size and configuration. Short runs were employed to reduce the chance of partial cluster breakup, especially at the higher temperatures. The results were then averaged to minimize statistical uncertainty. All vibrational free energies were computed based on a combination of the Quasi-Harmonic Approximation[41] at low temperature and thermodynamic integration[16] for higher temperatures. Further details of the simulation techniques employed in our calculations are given in ref. [20].

A. Initial Conditions and Cluster Geometry

The short time scale associated with MD simulation precludes full, long-range (i.e. diffusive) relaxation of cluster geometries. As a result, the choice of initial cluster geometry is critically important for making conclusions regarding nucleation and growth pathways[20,42,43]. Three distinct cluster growth modes, shown in Figure 2, were investigated in order to find the energetically favorable growth mode. The first two growth modes considered here are based on previous work by Bongiorno et al.[35]; these are the Hexagonal Ring Cluster (HRC) and the Spherically Shaped Cluster (SPC). HRC clusters are constructed based on the observed stability of the six-member ring and ten member cage bond structures in the diamond lattice. Spherically Shaped clusters are formed by the removal of atoms in concentric spherical shells around a

central atom. The third cluster growth mode investigated was the (111)-oriented stacking fault (SF), which consists of interconnected six-member vacancy rings arranged along a (111) plane. Also shown schematically in Figure 2 are the limiting, or macroscopic, shapes of clusters produced by each of the three growth modes. Note that the Hexagonal Ring cluster growth mode naturally leads to octahedral structures aligned along the (111) crystallographic planes.

B. Cluster Thermodynamics

The dominant cluster growth mode was determined by computing cluster formation enthalpies with MD in the temperature range $500 \leq T \leq 1600$ K for HRCs, SPCs, and SF clusters containing between one and thirty vacancies. The formation enthalpies for a cluster of size i was defined as $E_i^f = E(N-i) - [(N-i)/N]E_N$, where E_N is the enthalpy of a perfect lattice with N sites. The results of these calculations at 800 K are shown in Figure 3 and demonstrate clearly that the SF growth mode is not favorable relative to the HRC and SPC modes. Extrapolation of this conclusion to larger cluster sizes can be made readily, based on the linear scaling of the SF cluster energies as compared to the sub-linear scaling for Hexagonal Ring and Spherically Shaped clusters. The predicted high formation energy of Stacking Fault clusters is significant because other empirical Si potentials have been observed to predict the collapse of spheroidal vacancy clusters into stacking faults[43,44] at high temperatures.

The formation energies of Hexagonal Ring and Spherically Shaped clusters appear to approach each other for clusters containing about 18 vacancies. However, for smaller (and larger) clusters the HRC mode is found to be significantly more energetically favorable[20]. The

predicted stability of Hexagonal Ring clusters relative to Spherically Shaped clusters for these sizes is consistent with the predictions of tight binding molecular dynamics[32,35]. No simple functionality is apparent for the Spherically Shaped cluster formation energies in this size range, but it is expected that these energies will scale similarly to the HRC mode as cluster size increases and surface area-to-volume ratios evolve macroscopically, i.e. surface-area/volume ~ $1/r$, where r is a characteristic radius for the cluster.

The scaling behavior of the HRC formation enthalpy was investigated for larger clusters with MS. The 0 K enthalpies of formation show an approximately $n^{2/3}$ power-law scaling (actual exponent=0.64) that extends all the way to the very smallest clusters, indicating that an expression of the form $E_n^f(T) = \sigma(T)n^{2/3}$ is appropriate for capturing the 0 K enthalpic portion of the formation free energy for all Hexagonal Ring clusters. A comparison between (0 K) MS and 1000 K MD results for the formation energies of clusters up to size thirty shows that both sets of calculations give almost identical power-law fits[20] and indicate that (1) molecular statics are sufficient for capturing the local atomic, and (2) the temperature dependence of the formation enthalpy is essentially negligible.

Formation free energies and entropies for the Hexagonal Ring clusters in the size interval $1<N<35$ also were computed at temperatures ranging from 500 K to 1400 K. Interestingly, the formation free energies also are observed to scale approximately as $n^{2/3}$ at all temperatures as shown in Figure 4. Furthermore, the entropies of formation are entirely independent of temperature; see inset in Figure 4. These results of this thermodynamic analysis are used to fit an expression for the temperature dependent surface free energy for clusters[20]:

$$\gamma(T) = \left(2.76 - 4.44 \times 10^{-4} T\right) n^{2/3} \text{ eV}. \tag{3.1}$$

This expression is most accurate for clusters of size N>30 because smaller clusters deviate from the classical $n^{2/3}$ energy scaling behavior. For smaller clusters a correction must be added as discussed in ref. [20], and highlighted in Figure 4. An expression for vacancy cluster formation free energies therefore is proposed for the size interval $1 \leq N \leq 30$ and is given by

$$\gamma(T) = 3.23 n^{0.64} - T\left(4.34 \times 10^{-4} n^{0.67}\right) \text{ eV}, \tag{3.2}$$

where the two terms represent the formation enthalpies and entropies, respectively. Note that the entropic and enthalpic portions each are scaled to different power-law fits. This is necessary to maintain the validity of eq. (3.2) over the entire fitted temperature range, $500 \leq T \leq 1400$ K.

The EDIP potential predicts a thermodynamic melting temperature of about 1530 K[45]. However, a large amount of solid superheating (up to about 2200 K)[19] can be achieved in perfect crystals with periodic boundary conditions. The presence of defects such as vacancies lowers this limit somewhat. Our simulations at 1600 K in the superheated solid remain completely stable and demonstrate that the properties of single vacancies and clusters are well defined in the superheated region. While the EDIP crystal is thermodynamically metastable at this temperature, we find that even with large vacancy clusters, (for example a 165 vacancy HRC embedded in a lattice of 13,824 host atoms) the simulation cell can be annealed indefinitely at 1600 K without any melting as verified by rapid quenching using a conjugate gradient algorithm. Furthermore, simulations well into the superheated region (up to T=1800 K) indicate that cluster enthalpies

and the Arrhenius dependence of vacancy diffusion are unchanged from those at lower temperatures. The primary advantage of performing simulations at high temperatures is greatly accelerated evolution rates.

C. Equilibrium Cluster Size Distributions

The use of eqs. (3.1) and (3.2) for accurately representing cluster free energies in the size interval $1 \leq N \leq 30$ was investigated by computing equilibrium cluster size distributions with eqs. (3.1) and (3.2) and comparing them to the one generated using the actual values of the computed free energies of formation. In a thermodynamically open system, the equilibrium concentration of a cluster of size i, $C_i^{eq}(T)$, can be written as

$$C_i^{eq}(T) = z_i N_a \exp(-\frac{G_i^f}{kT}), \tag{3.3}$$

where, N_a is the number density of lattice sites, z_i is the number of possible ways of arranging the cluster on each lattice site and G_i^f is the formation free energy of the cluster. In an open system each cluster species can reach equilibrium independently of the other species in the system. In a closed system, however, the equilibrium cluster size distribution is determined by minimizing the total free energy subject to the constraint that the total number of vacancies is conserved, i.e. $\sum_i iX_i = N_V$, where N_V is the total number of single vacancies and X_i is the number of clusters of size i[46]. The total free energy of a closed system consisting of only vacancy defects is given by[47]

$$G = G_0 + \sum_i^{N_{\max}} X_i G_i^f - kT \sum_i^{N_{\max}} \left\{ X_i \ln i + \frac{N_s}{i} \ln(\frac{N_s}{i}) - \left[\frac{N_s}{i} - X_i \right] \ln \left[\frac{N_s}{i} - X_i \right] - X_i \ln X_i \right\}, \quad (3.4)$$

where G_0 is a reference free energy, defined here as the free energy of a perfect lattice with the same total number of lattice sites, N_s, as the defected system. N_{max} is the maximum cluster size considered in the minimization. The first term on the left-hand side of eq. (3.4) represents the reference free energy of the perfect crystal. The second term represents the vibrational free energy contributions of all clusters to the system, while the last summation gives the configurational entropy, and reflects the number of ways that an ensemble of clusters of different sizes can be arranged within the lattice.

The $\{G_i^f\}$ were determined using either eqs. (3.1) and (3.2) or the actual atomistic simulation data. In each case, the constrained minimization problem was solved with N_{max} = 30, $N_v = 1\times10^{15}$, and $N_s = 5\times10^{22}$. Figure 5 shows the three predicted equilibrium distributions of V_1, V_2, and V_{30} as a function of temperature. It can be seen clearly that while the predictions of eq. (3.1) deviate somewhat from the result obtained with the discrete atomistic values, eq. (3.2) provides an excellent representation of the cluster formation free energies as a function of temperature in the size interval $1 \le N \le 30$. For larger clusters, eq. (3.1) is expected to be accurate. A striking feature of Figure 5 is the sudden transition at a critical temperature between clustered and unclustered equilibrium size distributions. At high temperatures, entropic effects counteract the clustering energetic driving force and monomers are the dominant species, while at lower temperatures, V_{30} (the largest allowable in our simulation) become dominant. The transition temperature predicted by the atomistic data and eq. (3.2) is about 1350 K, while eq. (3.1) leads to

a value of about 1300 K. Although it is difficult to make a direct comparison with experimental conditions given the small value of N_{max} used here, the 1350 K value is in excellent agreement with the experimentally observed range of 1320-1370 K during crystal growth[48]. The appearance of larger clusters that would be detectable experimentally would occur at slightly lower temperatures, typically only a few degrees because aggregation is very rapid[49].

The error in the predicted melting temperature (i.e. 1530 K for EDIP versus 1685 K from experiments) does not necessarily affect the above comparison because the predicted (thermodynamic) melting temperature is a function of the accuracy of the potential in *both* the solid and liquid phases. Properties predicted in the solid phase should essentially be independent of how well a potential performs in the liquid state. In general, for a potential such as EDIP, which is parameterized primarily with respect to solid phases, it is to be expected that the solid-state free energy curve will be more accurate than the corresponding liquid-state one.

IV. VACANCY CLUSTER DIFFUSION

A common assumption[50,51] in the process modeling of solid-state aggregation of point defects and impurities in silicon is diffusion-limited growth by monomer addition (and dissociation). In the case of vacancy aggregation, the reaction pathway generally is expressed as a sequence of single-vacancy events

$$\cdots \xleftrightarrow{k_{N-1}} V_{N-1} + V_1 \xleftrightarrow{k_N} V_N + V_1 \xleftrightarrow{k_{N+1}} V_{N+1} + V_1 \xleftrightarrow{k_{N+2}} \ldots \tag{4.1}$$

where V_N denotes a vacancy cluster containing N vacancies and k_N represents the aggregation/dissolution rate of cluster V_N. The justification for this assumption typically is based on the assumed low concentration and diffusivity of dimers and larger vacancy clusters relative to single vacancies.

In this section, a detailed atomistic analysis of vacancy cluster diffusion rates and mechanisms is presented that demonstrates the mobility of small vacancy clusters and leads to quantitative estimates for their diffusivities. All diffusion simulations were performed using long MD runs of 6-20 million time steps (approx. 5-15 ns) in the NVT ensemble at 1600 K, corresponding to a timestep of approximately 0.8 fs. System sizes ranging from 216 to 1728 atoms were used, depending on the cluster size ($1 \leq N_V \leq 10$) under consideration. In addition, the temperature dependence of single vacancy and dimer diffusion was probed with simulations at temperatures ranging from 1300 K to 1650 K. The diffusion coefficient in each case was computed using the Einstein relation

$$D_N = \frac{1}{6} \frac{[r_N^{CM}(t) - r_N^{CM}(0)]^2}{t} \tag{4.2}$$

where $r_N^{CM}(t)$ is the center-of-mass of a cluster of size N. The center-of-mass (CM) for a vacancy cluster was computed first by locating the positions of each of the vacancies (see below) in the cluster, and then computing the average coordinates.

The use of a single CM trajectory to determine cluster diffusivity requires very lengthy simulations. In the case of single vacancy diffusion, a far better approach is to compute the total

mean-squared displacement (MSD) for the entire atomic system, which leads to a particle-averaged trajectory. However, the latter approach artificially increases estimates for cluster diffusion by including "internal diffusion" in which vacancies exchange positions with neighboring atoms (and hence increase the MSD) without leading to net cluster translation. The statistical efficiency of the CM mean-squared displacement calculations was increased substantially using the multiple time-origin approach[17]. In order to further reduce the error in the calculated diffusion coefficients five runs were performed for each cluster size.

A. Single vacancy Properties

The computed single vacancy diffusion coefficient is described well by the Arrhenius expression

$$D_V = 2.76\times10^{-4}\exp\left(-\frac{0.30eV}{kT}\right)\ cm^2/s\,, \tag{4.3}$$

and, in combination with the vacancy free energy for formation, leads to an estimate of the vacancy contribution to self-diffusion as

$$D_V C_V^{eq} = 6.28\times10^{21}\exp\left(-\frac{3.65eV}{kT}\right)\ cm^{-1}s^{-1}\,. \tag{4.4}$$

The predicted self-diffusion coefficient is in good agreement with estimates derived from metal diffusion experiments[52], especially at high temperature. For example, at 1600 K our value is 2.3×10^{10} $cm^{-1}s^{-1}$ which, compares reasonably well with the 6.12×10^{9} estimate of Bracht et al[52],

especially given the large uncertainty associated with these numbers in the literature. Interestingly, both the diffusion (0.3 eV) and formation (3.35 eV) activation energies are in excellent agreement with values regressed from metal diffusion experiments[53].

B. Cluster Diffusion

Vacancy cluster diffusion was analyzed using the CM mean-square displacement (eq. 4.1) and a vacancy-tracking algorithm to allow for dynamical structural analysis during diffusion. In general, cluster diffusion is expected to proceed via multiple transition (but still associated) states, as opposed to a single concerted event. Individual vacancies were tracked throughout each run by repeated monitoring of atomic positions. Any time an atom was found to be within 10 % of a bond length away from a previously known vacancy position, its position (on the perfect lattice at same density) was exchanged with the vacancy and the new vacancy position stored. The vacancy position data was used to compute a dynamic total inter-vacancy separation function, defined by

$$r_{sep}^{n} = \sqrt{\sum_{i}\sum_{j>i}\left(r_i - r_j\right)^2}\,, \tag{4.5}$$

where the summation indices, i and $j>i$, run over the number of vacancies in the cluster.

1. Vacancy Dimer Diffusion

The evolution of the separation function, r^{n}_{sep}, and the actual mean-square displacement of the vacancy dimer CM at 1600 K is shown in Figure 6. The separation function shows that the

divacancy alternates between three primary configurations as it diffuses within the silicon lattice. These separation function values, 2.35 Å, 3.85 Å and 4.57 Å, correspond to the nearest neighbor (NN), 2nd-nearest neighbor (2NN), and 3rd-nearest neighbor (3NN), configurations, respectively.

The separation function is observed to increase sharply beyond the 3NN value (4.57 Å) at about 0.3 ns; this event corresponds to dimer dissociation, and the evolution of the MSD in this region corresponds to the diffusion of two single vacancies. However, the confined simulation system and the positive binding free energy of the divacancy quickly lead to re-association of the dimer, and the dimer diffusion mechanism is observed once again. The computation of dimer (and other cluster) diffusion coefficients must be based only on the regions in which the diffusing cluster is associated. Shown in Figure 6 is the multiple time-origin averaged data in which dissociated dimer diffusion is removed, leading to a substantially lowered slope that would be obtained from a linear fit of the full MSD data.

The temperature dependent diffusion coefficient for V_2 is plotted in Figure 7 for the temperature range 1300<T<1650 K. The error bars in Figure 7 represent two standard deviations in each direction of the distribution of estimates at each temperature. The entire temperature range can be represented reasonably well with a single Arrhenius function with slope 1.45 eV. However, there is sufficient resolution in the data to suggest that a better interpretation is that the effective activation energy is higher at high temperature (~2 eV) and decreases (~1.3 eV) at lower temperatures.

The observed temperature dependence of the vacancy dimer diffusion coefficient was studied further by monitoring the time spent in each associated configuration as a function of temperature. It is shown in Figure 8 that most of the simulation time (>90 %) is spent in the nearest-neighbor (NN) configuration, with most of the remaining time spent in the 2NN configuration. However, it is important to note that the 3NN configuration still plays an important role in V_2 diffusion: the fact that far more time is spent in the NN and 2NN states indicates that the average residence time *per visit* is small for the 3NN configuration, but the actual *number of visits* is in fact comparable to the others (see Figure 6). Mechanistically, this implies that the observed temperature dependence should be a function of both the NN-2NN and 2NN-3NN transitions, which would support the hypothesized deviation from a simple Arrhenius curve shown in Figure 7. The time distribution among the three states is weakly dependent on temperature; the time fraction spent in state 3NN is largely unaffected by temperature and only the NN and 2NN ratios change as the cluster mobility increases. This is due to the strong driving force for regenerating the NN configuration, which has a very high binding energy of 1.61 eV relative to the isolated vacancies according to the EDIP potential. This value is in excellent agreement with previous estimates[54,55].

In order to determine the source of the high and possibly variable activation energy for vacancy dimer diffusion relative to single vacancy diffusion, a series of static relaxations were performed in which a vacancy dimer was allowed to relax in a host lattice under the constraint of fixed vacancy-vacancy separation. Single vacancy diffusion occurs via a direct path, with the split-vacancy representing the transition state. The energy barrier for this transition is given in eq. (4.3) as 0.3 eV, with identical initial and final configurations. On the other hand, vacancy

dimer diffusion is highly asymmetric; the energy profile as a function of separation for the dimer is shown in Figure 9 as the separation increases along the NN→2NN→3NN transition pathway. Several features of interest are apparent. First, the 2NN configuration is energetically unfavorable with respect to *both* the NN and 3NN configurations because the atom in between the two vacancies in the 2NN configuration must support two dangling bonds, rather than one per atom for the NN and 3NN configurations. Binding energies computed for distances higher than the 7.67 Å, i.e. the 4th neighbor distance along the (110) direction (4NN-110) are approximately zero. A detailed analysis of the capture distance between two vacancies is presented in a subsequent article.

The activation energy for the NN→2NN transition is about 2.5 eV. This interpretation is subject to the assumption that the narrow dip in the energy at 1.5NN in Figure 9 does not affect the kinetics of the transition from the NN to the 2NN dimer states. The observed local stability at exactly 1.5NN is due to the formation of a split-vacancy structure. The barrier for the 2NN→3NN transition is substantially lower, 1.3 eV, and results because of the high energy of the 2NN configuration. Therefore, a possible explanation for the observed temperature dependence in Figure 7 is that dimer diffusion is governed primarily by the 2NN→3NN transition at low temperature, where the NN→2NN transition becomes prohibitively slow because of its very high activation energy. At higher temperatures, the balance is shifted towards the NN→2NN transition, which becomes more important because of the overall stability of the NN configuration, i.e. the cluster is most often found in this state as seen in Figure 8.

2. Vacancy Trimer Diffusion

A similar analysis was performed for the vacancy trimer. The actual and averaged MSD and separation function, r_{sep}^{n}, for the vacancy trimer at 1600 K are shown in Figure 10. While the general trends are similar to the dimer case, the number of associated states during trimer diffusion increases to more than eight, although several of these have identical separation functions and only about five distinct values of the separation function can be identified. Once again, the cluster is observed to dissociate temporarily during the simulation but in each case quickly re-associates and continues to diffuse as a bound cluster.

The effect of temperature is more complex for trimer diffusion, as shown in Figure 11. Here, the energies of the different states are closer and exchange between them is more easily achieved. For temperatures below about 1400 K, the first two configurations (defined in terms of increasing separation function) dominate the diffusion process. At high temperatures, the trimer is observed to sample configurations with larger separation function more frequently as it becomes more mobile. The configurations of the various associated trimer states are shown in Figure 12 in order of increasing separation function from left to right. Each arrow in Figure 12 represents a reversible transition that requires the diffusion of a single atom (or vacancy). The energy value for each transition is taken as the energy difference between the two states at 0 K – all energy differences were computed by static minimization and do not include any additional barriers due to the formation of transition states. The mobility of vacancy clusters therefore can be understood in terms of the high degree of connectivity between the different associated states. The overall energy barrier for trimer diffusion should be reduced by the presence of these multiple pathways. For example, the transition from structure 1 to structure 2 in Figure 12, which

is the most energetically expensive, is not required for continued trimer diffusion; the trimer can diffuse indefinitely without ever visiting structure 1. This is consistent with the fact that in Figure 11, structure 1 is not the most visited configuration at high temperature. The key configuration in this case is structure 2, which can be regenerated via several, lower energy pathways.

3. Larger clusters

The dependence of cluster diffusivity on cluster size for larger clusters was investigated at 1600 K. Figure 13 shows diffusivities for clusters in the size range $1 \leq N \leq 10$ (solid line with error bars). Two important conclusions can be inferred from these results. The first is that cluster diffusion ($N>1$) can be described well by a single power-law with an exponent of about –1.25. This result is useful because it allows for extrapolation to larger cluster sizes, which also are expected to be mobile given the slow rate of decay shown in Figure 13. On the other hand, the single vacancy diffusion coefficient is substantially larger that would be predicted by extrapolating the observed power law behavior to N=1. The deviation of the single vacancy diffusion coefficient is easily explained by the results in the previous two sections: the single vacancy diffuses via a mechanism that does not involve the formation and destruction of vacancy-vacancy "bonds".

V. VACANCY AGGREGATION BY PARALLEL MOLECULAR DYNAMICS

The atomistic simulations described in Sections III and IV focus on the quantitative description of individual vacancy cluster thermodynamics and transport. Ideally, given a

sufficiently accurate interatomic potential, these estimates can be used directly as input into continuum models to predict vacancy aggregation dynamics under experimental conditions. Unfortunately, no empirical potential for silicon currently is accurate enough for such purposes[56]. In fact, even electronic structure calculations are still too uncertain for direct parameter estimation[57]. The aim of this Section is to bypass the requirement for a quantitatively predictive potential by using parallel molecular dynamics (PMD) to generate "experimental data" which with a continuum model can be compared in an internally consistent manner.

A PMD run was performed using a large cubic simulation cell consisting of 216,000 host silicon atoms arranged in a tetrahedral lattice from which 1,000 equally spaced vacancies were removed. The five million time step simulation (corresponding to about 4.5 ns of real time) was carried out in the NVT ensemble at 1600 K and approximately zero pressure. These conditions were chosen to give very high vacancy supersaturation and vacancy cluster diffusivities. During the course of the simulation, atomic coordinates for the entire system were stored at 1,000-80,000 time-step intervals. Each of these coordinate files then was used as a starting point for a rapid-quench MD simulation in which the temperature was lowered from 1600 K to 100 K in 3000 time steps. The quenched configurations were then compared to a reference perfect lattice at the same density in order to locate the vacancies in the system. Vacancy clusters then were identified using the Stillinger definition[58] that connects vacancies together based on their separation distances[59]. In this algorithm, a vacancy is used to identify a new cluster. Each time a new vacancy is found within its interaction range, it is added to the cluster. The neighbors of these vacancies are then found and so on, until all interacting vacancies are identified for each cluster.

The choice of cutoff distance for defining clusters is critical for a meaningful measure of the cluster size distribution. While the surface energy function presented in Section III (eq. 3.1) was based on the Hexagonal Ring cluster geometry in which each vacancy is adjacent to three others except at the cluster surface, it is clear that clusters are dynamically evolving structures, especially at high temperature. For example, the diffusing dimer was shown to alternate among three configurations: NN, 2NN, and 3NN. A snapshot in time could potentially find the dimer in any of these three configurations. A restrictive definition of a cluster based only on NN interactions would mistakenly identify the dimer as two single vacancies unless it was captured in the NN configuration. In other words, the cutoff distance for defining clusters must be chosen consistently to encompass the interaction range between vacancies. The average cluster size evolution was computed based on 2NN, 3NN, and 4NN-110 (4th-nearest neighbor along the 110 direction) cutoff distances. The 2NN criterion for defining associated clusters significantly under-predicted the evolution dynamics, but both the 3NN and 4NN-110 definitions were found to give the same cluster size distribution for the entire simulation. The 4NN-110 cut-off is used for all results discussed in this work.

The transient size distribution was analyzed by computing moments according to the general expression

$$M_n = \sum_s s^n X_s \tag{5.1}$$

where X_s is the number of clusters of size s, and n is the moment order. Thus, the 0th moment (M_0) corresponds to the total number of clusters, and the ratio of the of the 2nd and 1st moments

(M_2/M_1) is a measure of the average cluster size. These quantities and the concentration of single vacancies are plotted as a function of time in Figure 14. Also shown are power law fits to each of these quantities. All are observed to fit well to power laws after an initial period of about 0.1 ns. The exponents are -0.39 for the total cluster number (M_0), 0.39 for the average cluster size (M_2/M_1) and –0.81 for the monomer number (X_1).

VI. MEAN-FIELD SCALING ANALYSIS

The power-law evolution of the vacancy cluster size distribution suggests that a mean-field scaling analysis should be applicable. Family et al.[60] have shown that a transient analysis of the Smoluchowski equation can be performed analytically by assuming a scaling form for the size distribution. The approach has been generalized by Sorensen et al.[61] to include a broader description of the aggregation/fragmentation kernels. The Smoluchowski equation is written as

$$\frac{dX_k}{dt} = \frac{1}{2}\sum_{i+j=k}\left[K(i,j)X_iX_j - F(i,j)X_{i+j}\right] - \sum_{j=1}^{\infty}\left[K(k,j)X_kX_j - F(k,j)X_{k+j}\right], \qquad (6.1)$$

where X_k is the number of clusters of size k, $K(i,j)$ is the coagulation kernel between two clusters of size i and j, respectively, and $F(i,j)$ is the fragmentation kernel, which describes the rate of dissociation of a cluster of size $i+j$ into two clusters of size i and j, respectively. Assuming that the coagulation and fragmentation kernels are homogeneous, i.e. $K(ai,aj) = a^{\lambda}K(i,j)$ and $F(ai,aj) = a^{\alpha}F(i,j)$, and using the following scaling form for size distribution

$$n(i,t) = M_1 s(t)^{-2} \phi(i / s(t)) , \tag{6.2}$$

where *s(t)* is the average cluster size, defined as (M_2/M_1), eq. (6.1) can be written as[61]

$$\frac{ds^*}{dt^*} = s^{*\lambda} - s^{*(\alpha+2)} . \tag{6.3}$$

In eq. (6.3), $s^*=s(t)/s_0$, and $t^*=t/t_0$, where s_0 is the equilibrium value of the average cluster size, and t_0 is the characteristic time for the size distribution to reach equilibrium. For very small times, i.e. when $s^*<<1$, the solution of eq. (6.3) is given by

$$s^* = \left[(1-\lambda)t^* + s_i^{*(1-\lambda)}\right]^z , \tag{6.4}$$

where $s_i^* = s\ (t=0)/s_0$ is the scaled initial value of the mean cluster size, and $z = 1/(1-\lambda)$. Thus, if s_i^* is sufficiently small, $s^* \sim t^z$ at small times. However, if s_i^* is large, i.e. the initial mean cluster size is not much smaller than the equilibrium value, s_0, this scaling behavior will not appear because the second term on the left-hand side of eq. (6.3) becomes significant before t^* is large enough to make s_i^* negligible.

The evolution of M_2/M_1 in Figure 14 is qualitatively consistent with the form of eq. (6.3). At very small times (t < 0.01 ns), a flat profile is observed, and in this region s_i^* is dominant. For t>0.1 ns, the first term in eq. (6.4) becomes dominant and a power scaling is observed, consistent

with the analyses in refs. [60] and [61], and also with a small value of s_i^*. Using a detailed mean-field simulation of the vacancy aggregation process (to be described in detail in a future publication), we estimate that the limiting value of the mean cluster size, $s_0 = s(t \to \infty)$, approaches 200 and therefore $s_i^* \sim 5 \times 10^{-3}$ for the system represented in the PMD simulation. This small value is consistent with the short initial transient in Figure 14.

In order to make quantitative conclusions regarding the actual value of the exponent for M_2/M_1, a kinetic (and homogeneous) form for the coagulation kernel, $K(i,j)$, must be postulated. In the following, we assume that the PMD timescale is sufficiently small so that we do not need to consider the fragmentation problem. This assumption is justified below. Using diffusion-limited aggregation theory[62,63], $K(i,j)$ is written as

$$K(i,j) \sim (D_i + D_j)(r_i + r_j)^2, \tag{6.5}$$

where r_x and D_x ($x=i,j$) are the radius and diffusivity, respectively, of a cluster of size x. The second term on the right-hand side of eq. (6.5) represents the total capture radius for the aggregation of clusters i and j, which is expected to be proportional to the sum of the radii of the interacting clusters. The form of eq. (6.5) implicitly assumes that no activation barrier for coagulation exists, which is a good assumption for highly supersaturated systems at early times where a high driving force for aggregation exists. The existence of an activation energy barrier for the aggregation and dissolution kernels will be discussed further in a future publication. A similar expression can be written for the coagulation of clusters of size γi and γj so that

$$K(\gamma i, \gamma j) \sim \gamma^{2/3}(D_{\gamma i} + D_{\gamma j})(r_i + r_j)\,. \tag{6.6}$$

In eq. (6.6) it is assumed that the clusters are approximately spherical and therefore $r \sim n^{1/3}$. If the diffusion coefficients also are assumed to be homogeneous, i.e. $D_{\gamma i} = \gamma^p D_i$, then the coagulation kernels are homogeneous overall, i.e.

$$K(\gamma i, \gamma j) = \gamma^{p+2/3} K(i, j)\,. \tag{6.7}$$

The growth exponent for the mean cluster size, M_2/M_1, in Figure 14 was given as 0.39, which leads to an estimate for $\lambda = p + 2/3 = -1.56$, or $p \sim -2.23$ This predicted decay for the cluster diffusion coefficient as a function of size is plotted along with the actual cluster diffusion coefficients in Figure 13. The mean-field diffusion coefficient decay is essentially a single power-law fit of the actual diffusion coefficients.

The interpretation of our atomistic simulation results in the context of a simple scaling theory was tested by comparing the results in Figure 14 directly to eq. (6.4) with $\lambda = -1.56$, $t_0 = 1 \times 10^{-5}$ s, and $s_0 = 200$. The solution of eq. (6.3) and the MD results for M_2/M_1 are shown in Figure 15. Note that the solution represented by eq. (6.4) has been expressed in dimensional units of seconds and total vacancy number, so that a direct comparison with the MD results could be made. Clearly, the agreement is excellent not only for the power law region (which is determined solely by the fit value of λ), but also in the initial transient. The overall agreement is evidence that our estimates for s_0 and t_0 are correct and that the interpretation of the atomistic

simulation results in terms of a simple scaling theory is justified. Of course, no conclusions can be made for longer times based on this analysis because we have neglected the process of fragmentation in Figure 15. Furthermore, the average cluster size is a single moment of the entire cluster size distribution and it is unlikely that a highly simplified analysis such as the one above is capable of reproducing finer details of the cluster size distribution, such as the number of individual cluster sizes as a function of time. These additional components will be considered explicitly in a full mean-field model in ref. [64].

VII. CONCLUSIONS

A comprehensive atomistic analysis of vacancy cluster diffusion and aggregation in crystalline silicon was performed using the EDIP potential and state-of-the-art large-scale parallel molecular dynamics. The length and time scales accessed by molecular dynamics in this work enabled a direct analysis of the size distribution evolution with mean-field theory. The diffusion of small vacancy clusters is found to be an important mechanism in setting the evolution during vacancy aggregation. A closed form expression for the free energy of vacancy clusters also was developed and was demonstrated to represent well the equilibrium properties of HRC vacancy clusters, which have been shown to be the most stable cluster morphology predicted by the EDIP potential. These findings are entirely consistent with more detailed electronic structure calculations, as well as the experimentally observed octahedral structure of large vacancy clusters.

The molecular dynamics results for the evolution of the vacancy cluster size distribution were interpreted in terms of a simple mean-field scaling analysis, which demonstrates explicitly the contribution of cluster diffusion to the overall evolution dynamics. It is expected that vacancy cluster diffusion also will be important in the accurate continuum modeling of defect evolution during actual crystal growth and high temperature wafer processing because vacancy clustering is observed to initiate at high temperature (1450 K) during crystal growth. Furthermore, the interplay between mobile monomers, dimers, and other small clusters could affect the balance between vacancies and other point defects, such as self-interstitials and dopants. These studies will be presented in a future publication. The results in this paper should be instrumental in developing a highly accurate and predictive model for vacancy aggregation in silicon. Furthermore, the overall approach presented here should be applicable to the study of more complex aggregation phenomena, such as the co-aggregation of multiple species, where continuum models are generally more difficult to pose.

ACKNOWLEDGEMENTS

This work was supported by an NSF CAREER Award (CTS01-34418), Wacker Siltronic AG, and the ACS Petroleum Research Fund (PRF #36923-G5). We would also like to thank John Crocker for many fruitful discussions along the way.

REFERENCES

1 H. Föll, U. Gösele and B. O. Kolbesen, J. Cryst. Growth, 52, 907 (1981).

2 R. Falster, V. V. Voronkov and F. Quast, Phys. Stat. Sol. (B) 222, 219 (2000).

3 H. Hieslmair, S. Balasubramanian, A. A. Istratov, and E. R. Weber, Semicond. Sci. Technol. **16**, 567 (2001).

4 J. Tersoff, C. Teichert, and M. G. Lagally, Phys. Rev. Lett. **76**, 1675 (1996).

5 T. R. Mattsson, and H. Metiu, Appl. Phys. Lett. **75**, 926 (1999).

6 P. M. Fahey, P. B. Griffin, and J. D. Plummer, Rev. Mod. Phys. **61**, 289 (1989).

7 T. Y. Tan and U. M. Gösele, Appl. Phys. A. **37**, 1 (1985).

8 T. Sinno, E. Dornberger, W. von Ammon, R. A. Brown, and F. Dupret, Mat. Sci. Eng. R **28**, 149 (2000).

9 W. Bergholz, and D. Giles, Phys. Stat. Sol. B **222**, 5 (2000).

10 T. Sinno, R. A. Brown, W. von Ammon, and E. Dornberger, J. Electrochem. Soc. **145**, 302 (1998).

11 E. Dornberger and W. von Ammon, J. Electrochem. Soc., **143** 1648 (1996).

12 R. Falster, and V. V. Voronkov, Mat. Sci. Engg. B **73**, 87 (2000).

13 W. von Ammon, E. Dornberger, H. Oelkrug, and H. Widener, J. Cryst. Growth, **151**, 273 (1995).

14 A. La Magna, and S. Coffa, Comput. Mat. Sci. **17**, 21 (2000).

15 M. Jaraiz, L. Pelaz, E. Rubio, J. Barbolla, G. H. Gilmer, D. J. Eaglesham, H.-J. Gossmann, J. M. Poate, Mater. Res. Soc. Proc. **568** 43 (1998).

16 M. P Allen, and D. J. Tildesley, *Computer Simulations of Liquids* (Clarendon Press, Oxford, 1987).

17 D. Frenkel and B. Smit, *Understanding Molecular Simulation* (Academic Press, San Diego, 1996).

18 M. Z. Bazant, E. Kaxiras, J. F. Justo, Phys. Rev. B **56** 8542 (1997).

19 J. F. Justo, M. Z. Bazant, E. Kaxiras, V. V. Bulatov, and S. Yip, Phys. Rev. B **58**, 2359 (1998).

20 M. Prasad, and T. Sinno, Appl. Phys. Lett. **80**, 1951 (2002).

21 M. von Smoluchowski, Z. Phys. Chem, **92**, 129 (1917); Phys. Z. **17**, 583 (1916).

22 H. Risken, *The Fokker-Planck Equation: Methods of Solutions and Applications* (Springer-Verlag, Berlin, New York, 1989).

23 E. Dornberger, D. Temmler, and W. von Ammon, J. Electrochem Soc. **149** G226 (2002).

24 R. Winkler, and G. Behnke, in *Semiconductor Silicon* **94**, edited by H. R. Huff, W. Berghol, and K. Sumino, The Electrochemical Society, Pennington, New Jersey, 1994, p. 673.

25 M. Itsumi, H. Akiya, T. Ueki, M. Tomita, and M. Yamawaki, J. Appl. Phys. **78**, 5984 (1995).

26 D. J. Eaglesham, A. E. White, L. C. Feldman, and D. C. Jacobson, Phys. Rev. Lett. **70**, 1643 (1993).

27 H. Rucker, B. Heinemann, and R. Kurps, Phys. Rev. B **64**, 073202 (2001).

28 J. Tersoff, Phys. Rev. B **64**, 1757 (1990).

29 T. Sinno, and R. A. Brown, J. Electrochem. Soc. **146**, 2300 (1999).

30 E. Dornberger, J.Esfandyari, J. Vanhellemont, D. Graf, U. Lambert, F. Dupret, W. von Ammon, *Proceedings of the Eighth International Symposium on Silicon Materials Science and Technology: Silicon Materials Science and Technology* **1**, The Electrochemical Society, Pennington, New Jersey, 1998, p. 490.

31 K. Nakamura, T. Saishoji, T. Kubota, T. Iiada, Y. Shimanuki, R. Kotooka, and J. Tamioka, J. Cryst. Growth **180**, 61 (1997).

32 G. D. Watkins and J. W. Corbett, Phys. Rev. **138**, A543 (1965).

33 J. L. Benton, S. Libertino, P. Kringhøj, D. J. Eaglesham, J. M. Poate, and S. Coffa, J. Appl. Phys. **82**, 120 (1997).

34 M. Huang, Y. Wang, J. Yang, Y. He, Y. Guo, and C. Liu, Mater. Sci. Forum **105-110**, 1071 (1992).

35 A. Bongiorno, L. Colombo, T. D. De La Rubia, Europhys. Lett. **43**, 695 (1998).

36 T. E. M. Staab, A. Sieck, M. Haugk, M. J. Puska, Th. Frauenheim, and H. S. Leipner, Phys. Rev. B **65**, 115210 (2002).

37 D. J. Chadi, and K. J. Chang, Phys. Rev. B **38**, 1523 (1988).

38 A. La Magna, S. Coffa, and L. Columbo, Nucl. Instr. Meth. Phys. Res. B **148**, 262 (1999).

39 S. K. Estreicher, J. L. Hastings, and P. A. Fedders, Appl. Phys. Lett. **70**, 432 (1997).

40 G. J. Martyna, D. J. Tobias, and M. L. Klein, J. Chem. Phys. **101,** 4177 (1994).

41 W. G. Hoover, A. C. Hindmarsh, and B. L. Holian, J. Chem. Phys. **57,** 1980 (1972).

42 N. Cuendet, T. Halicioglu, and W. A. Tiller, App. Phys. Lett. **67**, 1063 (1995).

43 T. Y. Tan, P. Plekhanov, and U. M. Gosele, Appl. Phys. Lett. **70,** 1715 (1997).

44 G. Sin, Ph. D. Thesis, MIT (2000).

45 P. Keblinski, M. Z. Bazant, R. K. Dash, and M. M. Treacy, Phys. Rev. B, **66**, 64104 (2002).

46 L. A. Girifalco, *Statistical Mechanics of Solids*. (Oxford Press, New York 2000)

47 J. L. Katz and H. weidersich, J. Chem. Phys. **55**, 1414 (1971).

48 M. Hourai, T. Nagashima, E. Kajita, S. Miki, S. Sumita, M. Sano, T. Shigematsu, and H. R. Huff in *Semiconductor Silicon* **94-10***,* edited by H. R. Huff, W. Berghol, and K. Sumino, The Electrochemical Society, Pennington, New Jersey, 1994, p. 156.

49 V. V. Voronkov, and R. Falster, J. Cryst. Growth **194**, 76 (1998).

50 T. Sinno, and R. A. Brown, J. Electrochem. Soc. **146**, 2300 (1999).

51 J. Esfandyari, C. Schmeiser, S. Senkader, G. Hobler, and B. Murphy, J. Electrochem. Soc. **143**, 995 (1996).

52 H. Bracht, in *Defects in Silicon III* **99-1**, edited by T. Abe, W. M. Bullis, S. Kobayashi, W. Lin, and P. Wagner, The Electrochemical Society, Pennington, New Jersey, 1999, p. 357.

53 H. Bracht, N. A. Stolwijk, and H. Mehrer, Phys. Rev. B, **52** (1995) 16542.

54 J. A. van Vechten, Phys. Rev B, **33**, 2674 (1986).

55 L. J. Cheng, J. C. Corelli, J. W. Corbett, and G. D. Watkins, Phys. Rev. **152**, 761 (1966).

56 H. Balamane,T. Halicioglu, and W. A. Tiller, Phys. Rev. B, **46**, 2250 (1992).

57 T. Sinno, Thermophyiscal properties of intrinsic point defects in crystalline silicon, in press: Proc. Electrochem. Soc. (2002).

58 F. H. Stillinger, J. Chem. Phys., 38, 1486 (1963).

59 F. K. von Gottberg, Ph. D. Thesis, MIT (1997).

60 F. Family, P. Meakin, and J. M. Deutch, Phys. Rev. Lett. **57**, 727 (1986).

61 C. M. Sorensen, H. X. Zhang, and T. W. Taylor, Phys. Rev. Lett. **59**, 363 (1987).

62 F. S. Ham, J. Phys. Chem. Solids **6**, 335 (1958)

63 M. Schrems M, P. Pongratz, M. Budil, H. W. Potzl, J. Hage, E. Guerrero, D. Huber, *Proceedings of the Sixth International Symposium on Silicon Materials Science and Technology: Semiconductor Silicon 1990*, The Electrochemical Society, Pennington, New Jersey, p. 144

64 M. Prasad and T. Sinno, to be published.

FIG. 1: An integrated, internally consistent approach for mechanistic and parametric investigations of solid-state aggregation.

FIG. 2: (1) HRC, (2) SPC, and (3) (111)-SF vacancy cluster growth modes in the silicon lattice. Shown are the HRC-6, 10, 14, and 35 clusters, the SPC-6, 10, 14, and 35 clusters, and the SF-6, 10, 13, and 24 clusters.

FIG 3: Enthalpies of formation for HRC (squares and solid line), SPC (circles) and SF (diamonds and solid line) vacancy clusters at 800 K. The HRC clusters are favored over the other two growth modes. Error bars are approximately the size of the symbols.

FIG. 4: Formation free energies for HRC clusters in the size interval $1<N<35$ at 500 K (triangles) and 1400 K (circles). Solid lines are optimal power fits (exp. = 0.62), dashed lines are $n^{2/3}$ fits. Inset: Formation entropies averaged over entire temperature range. Power law fit (solid line) and $n^{2/3}$ fit (dashed line) give identical results.

FIG. 5: Equilibrium concentrations of V_1 (squares), V_2 (circles), and V_{30} (diamonds) species as a function of temperature. The three sets of data shown are for free energies computed from eq. (3.1) (short dash lines), eq. (3.2) (long dash lines), and full atomistic results (solid lines). The vertical line shows the nucleation temperature predicted by eq. (3.2) and the discrete atomistic free energies.

FIG. 6: Center-of-Mass Mean-square displacement (CM-MSD) and inter-vacancy separation function (solid squares) for the vacancy dimer at 1600 K. Also shown is the averaged CM-MSD (dashed line).

FIG. 7: Arrhenius plot for the V_2 diffusion coefficient. Solid line represents a single Arrhenius fit, while the two dashed lines show possible activation energy variation with temperature.

FIG. 8: Residence time fraction spent in each associated state during dimer diffusion at 1200 K (squares), 1500 K (circles), and 1600 K (triangles).

FIG. 9: Statically relaxed formation energies of dimer configurations along the NN→2NN→3NN transition.

FIG. 10: Center-of-Mass Mean-square displacement (CM-MSD) and inter-vacancy separation function (solid squares) for the vacancy trimer at 1600 K. Also shown is the averaged CM-MSD (dashed line).

FIG. 11: Residence time fraction spent in each associated state during vacancy trimer diffusion at 1200 K (squares), 1400 K (circles), and 1600 K (triangles).

FIG. 12: Configurations of seven individual associated states involved in the diffusion of vacancy trimers (light-spheres are vacancies, dark ones are Si atoms). The separation

function increases from left to right: values are 2.42, 3.03, 3.17, and 3.54 (A/σ). Also shown are the elementary transition pathways (arrows). Energy differences are for transitions from lower label to higher label: e.g $E_{1\rightarrow 2}$ = +1.93 eV.

FIG. 13: Diffusion coefficients for vacancy clusters as a function of cluster size at 1600 K. Solid line and squares – EDIP predictions; dashed line and diamonds – mean-field model fit.

FIG. 14: Temporal evolution of M_0 (squares), M_2/M_1 (circles), and X_1 (diamonds). Power law fits (for t > 0.1 ns) give exponents of –0.39, +0.39, and –0.81, respectively.

FIG. 15: Evolution of $s^*(t)$ as a function of time. Squares: direct atomistic simulation; Solid Line: solution of eq. (6.3).

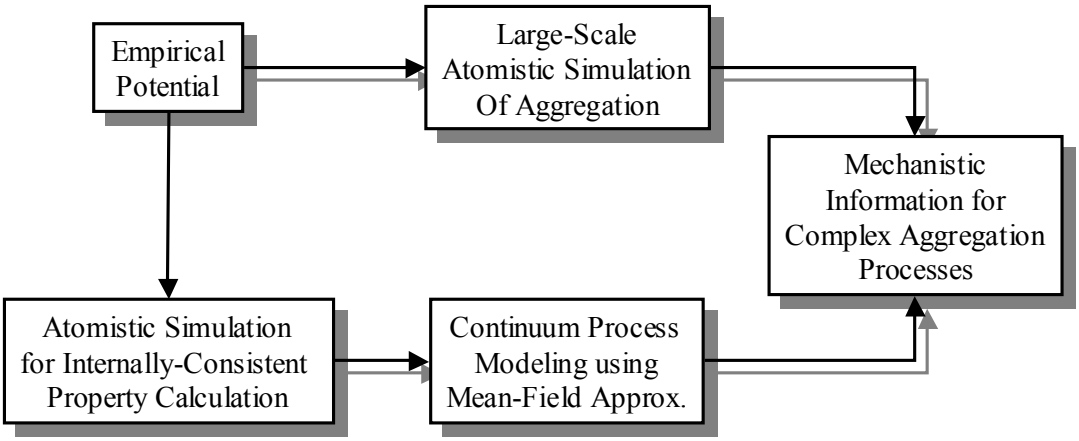

FIG. 1: Prasad and Sinno

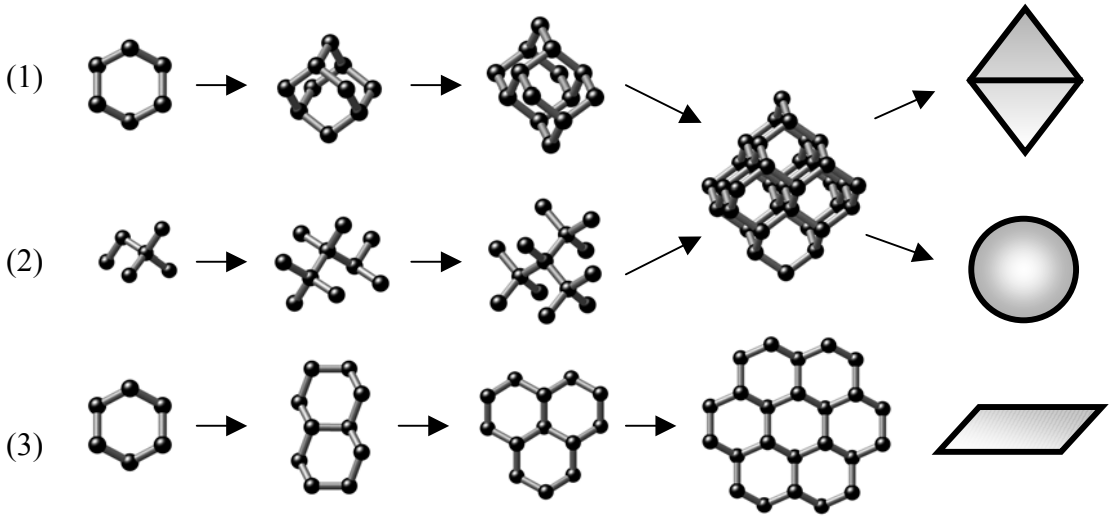

FIG. 2: Prasad and Sinno

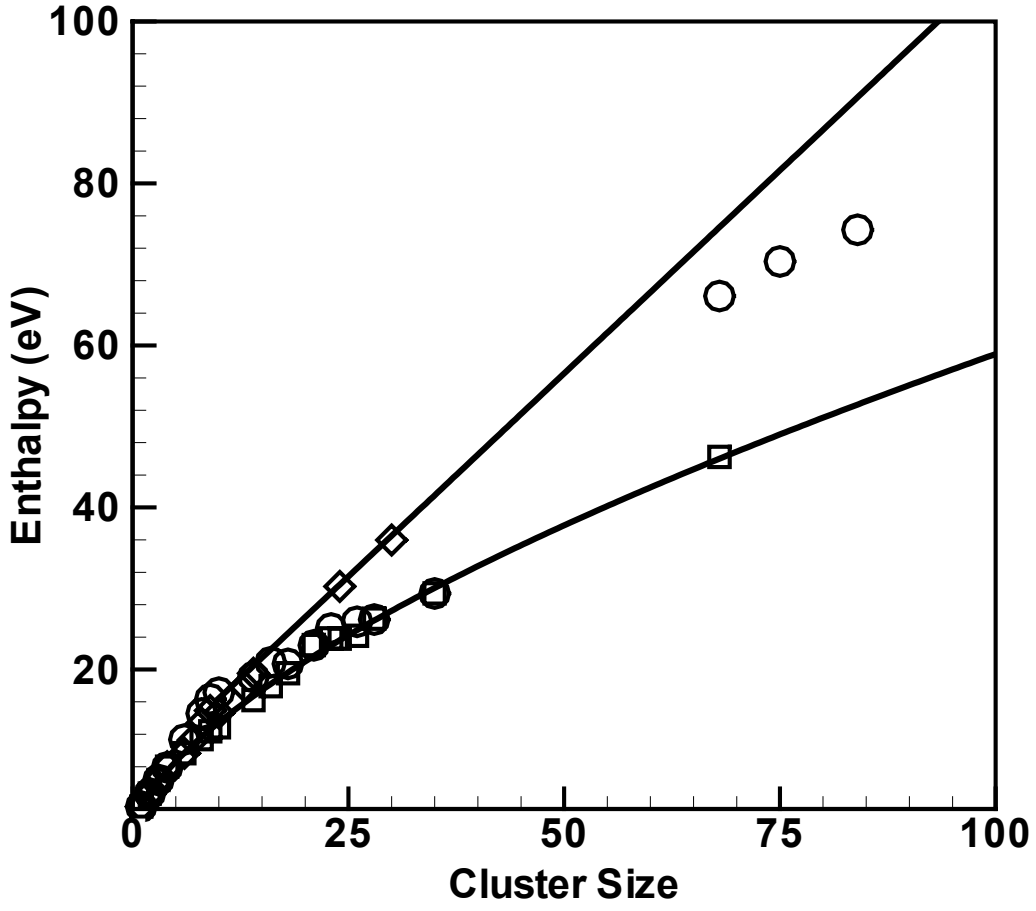

FIG 3: Prasad and Sinno

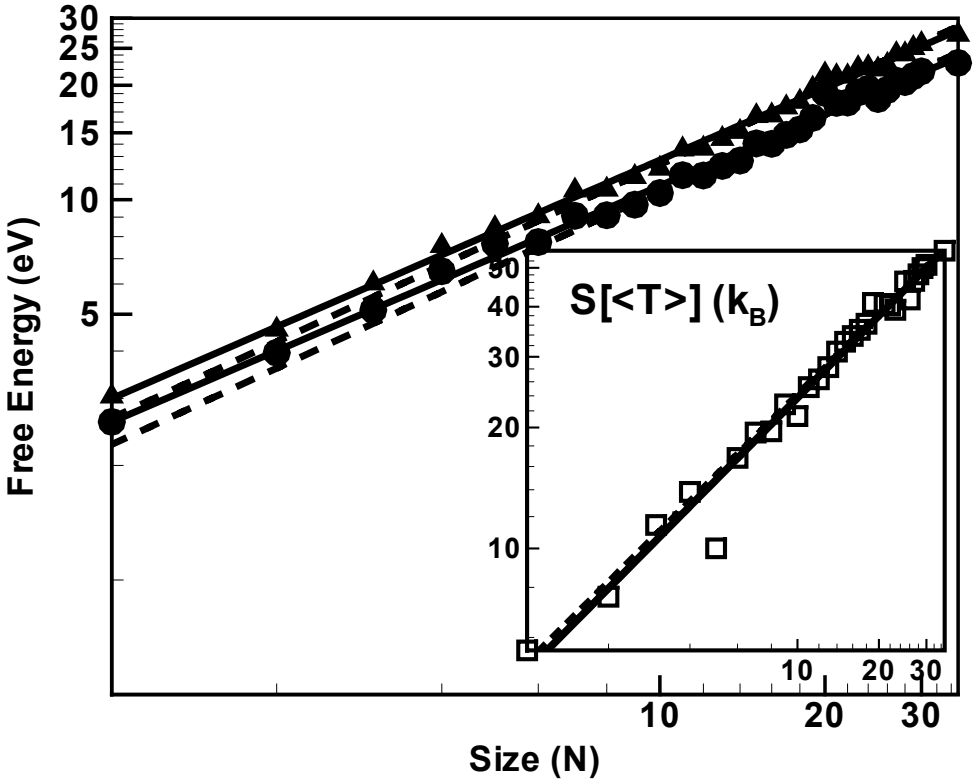

FIG. 4: Prasad and Sinno

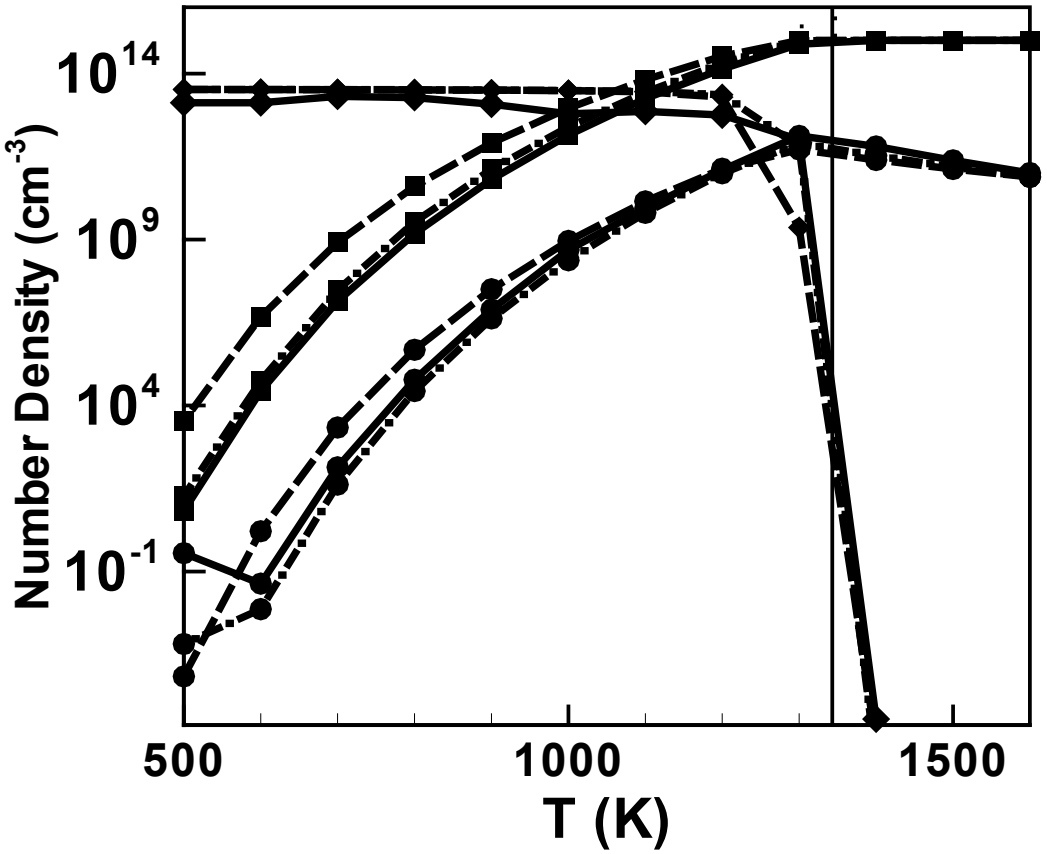

FIG. 5: Prasad and Sinno

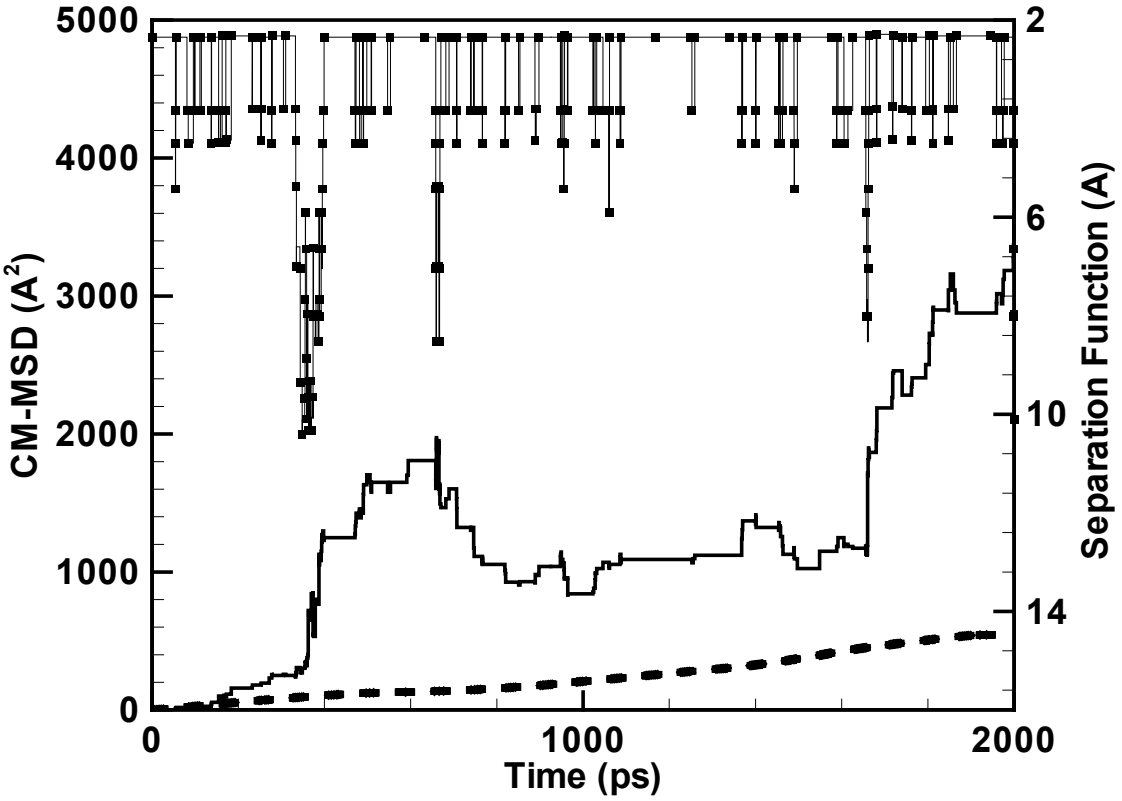

FIG. 6: Prasad and Sinno

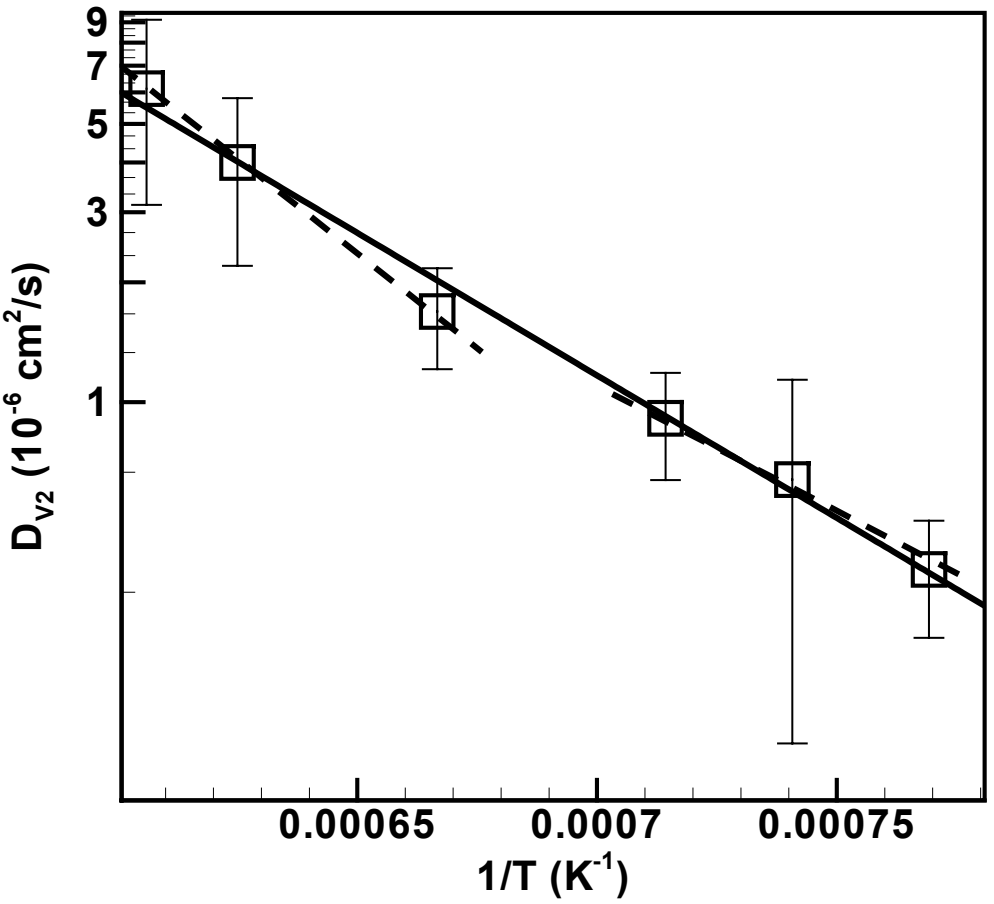

FIG. 7: Prasad and Sinno

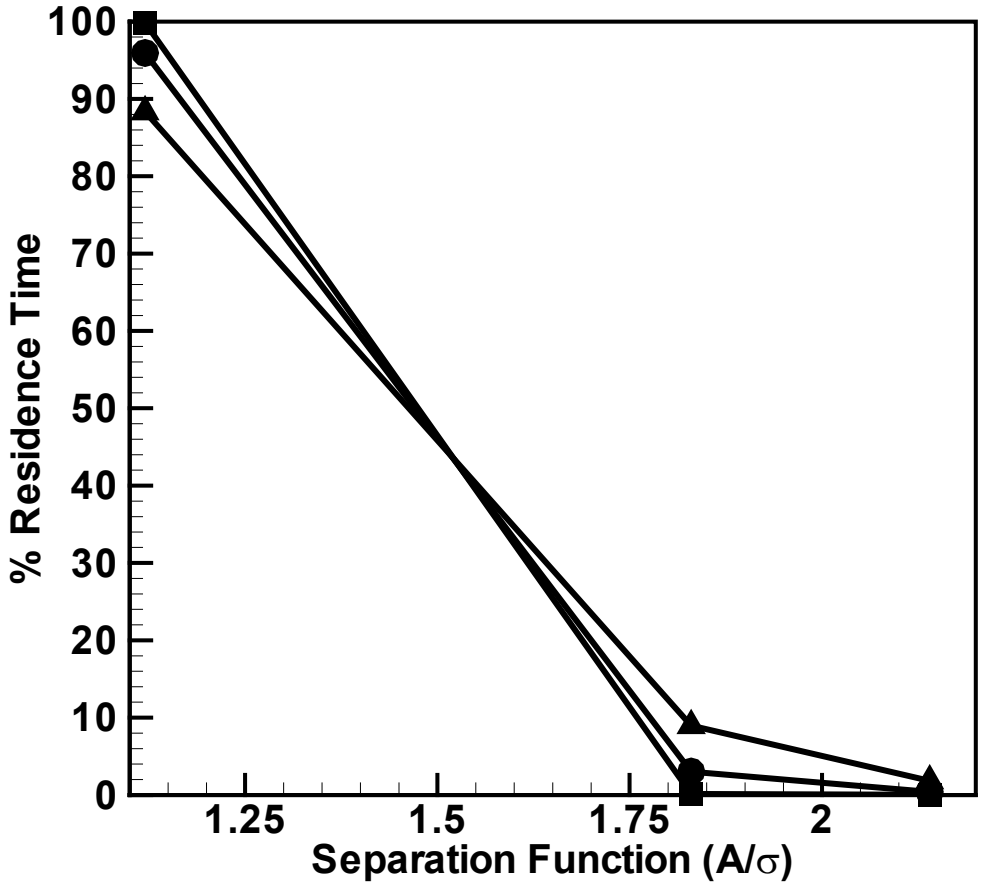

FIG. 8: Prasad and Sinno

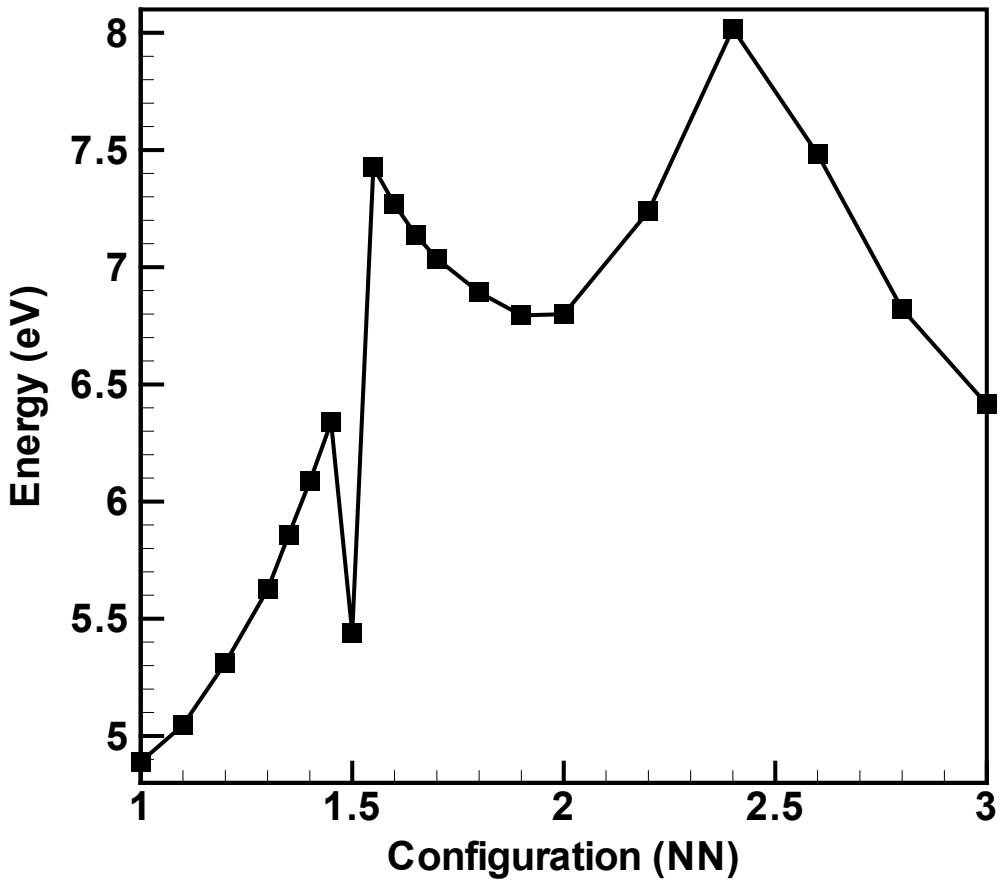

FIG. 9: Prasad and Sinno

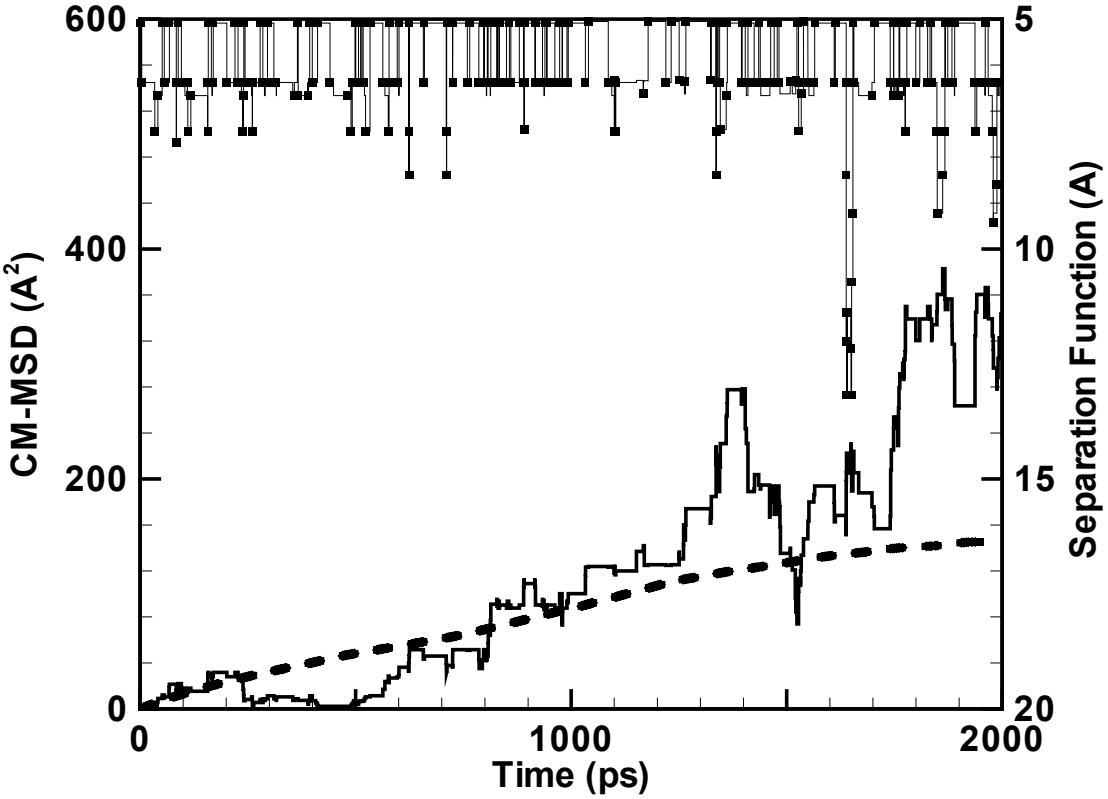

FIG. 10: Prasad and Sinno

.

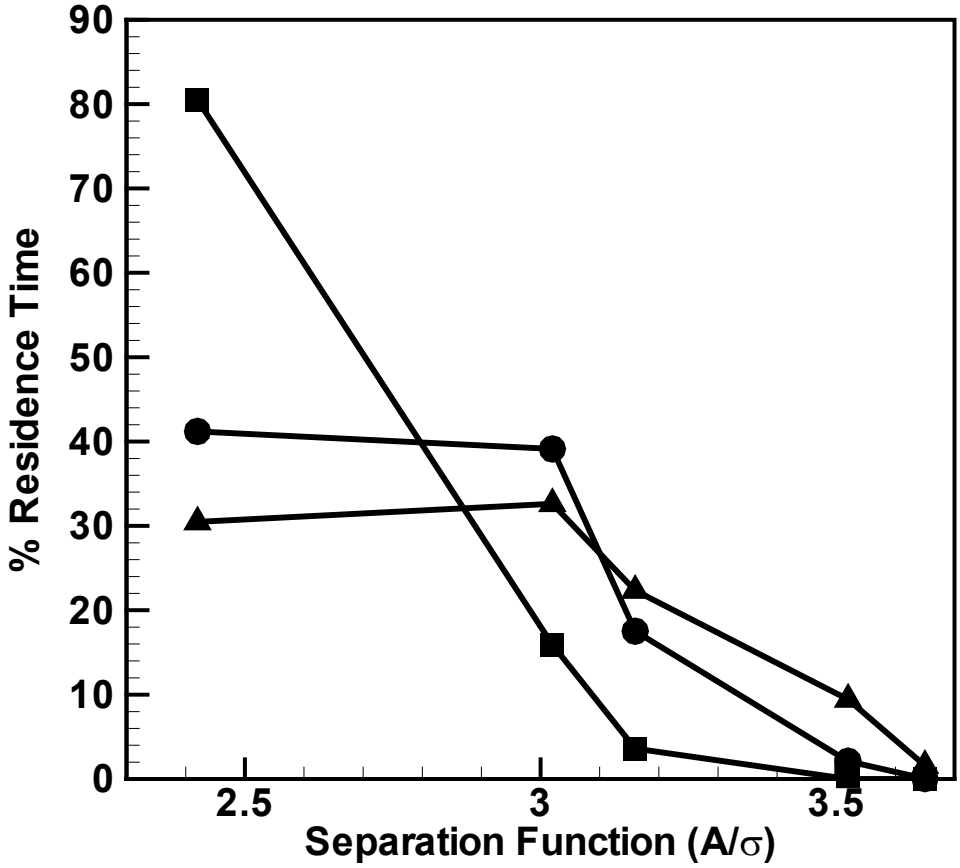

FIG 11: Prasad and Sinno

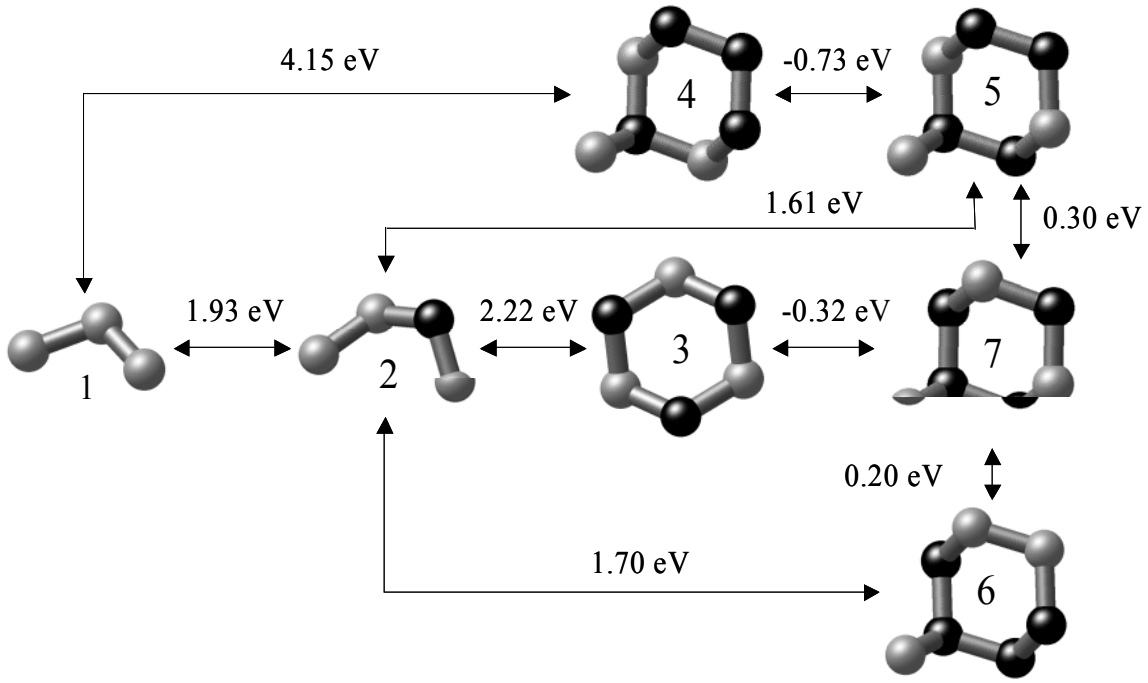

FIG. 12: Prasad and Sinno

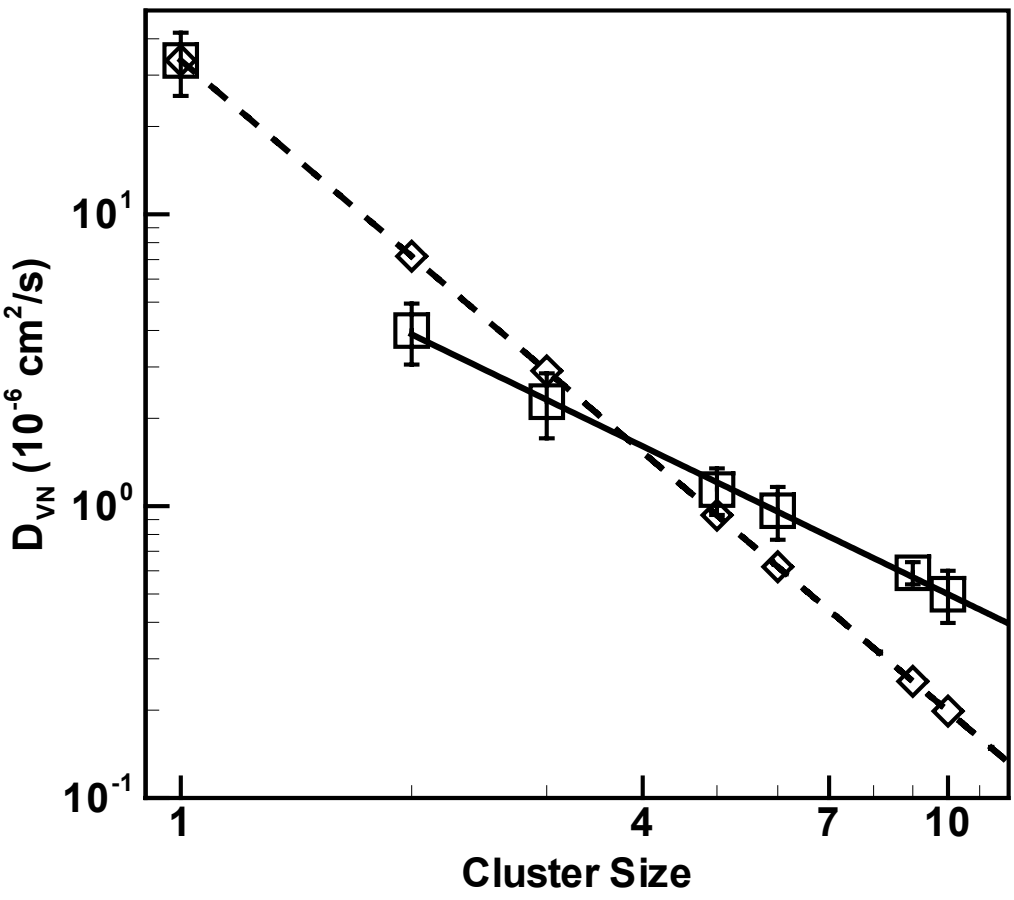

FIG. 13: Prasad and Sinno

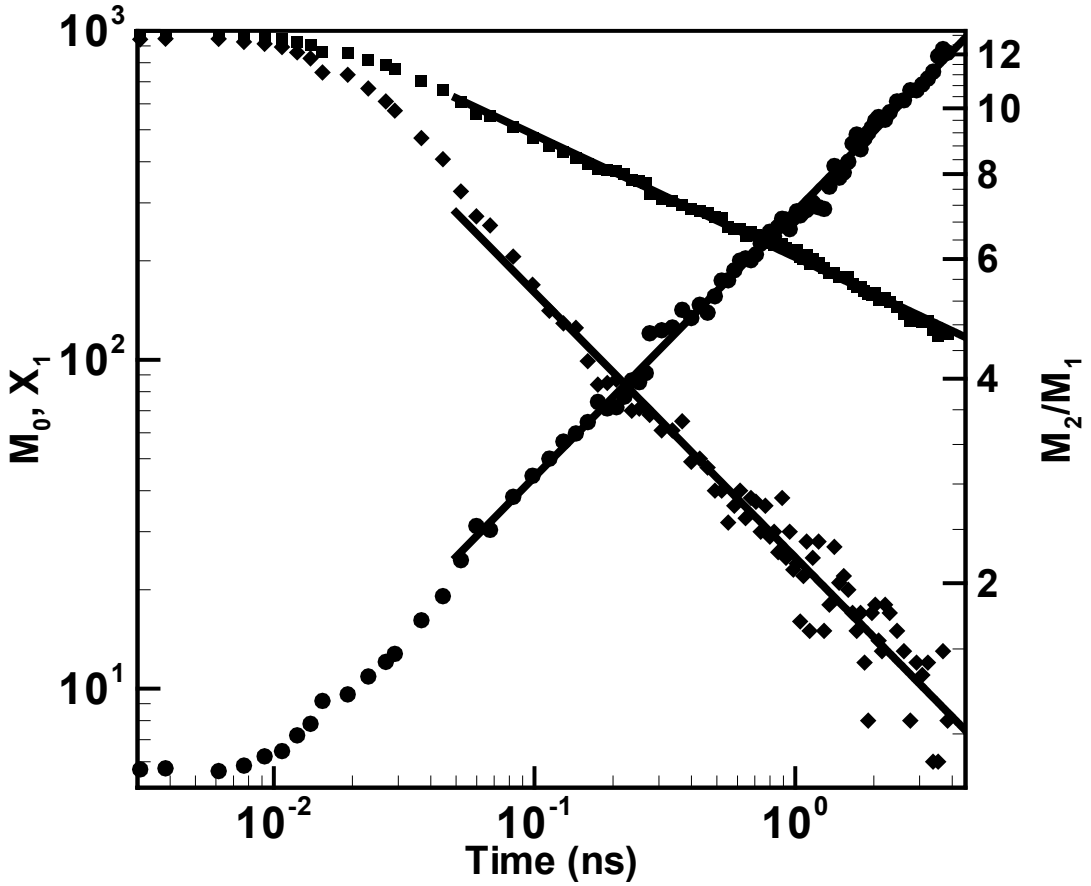

FIG 14: Prasad and Sinno

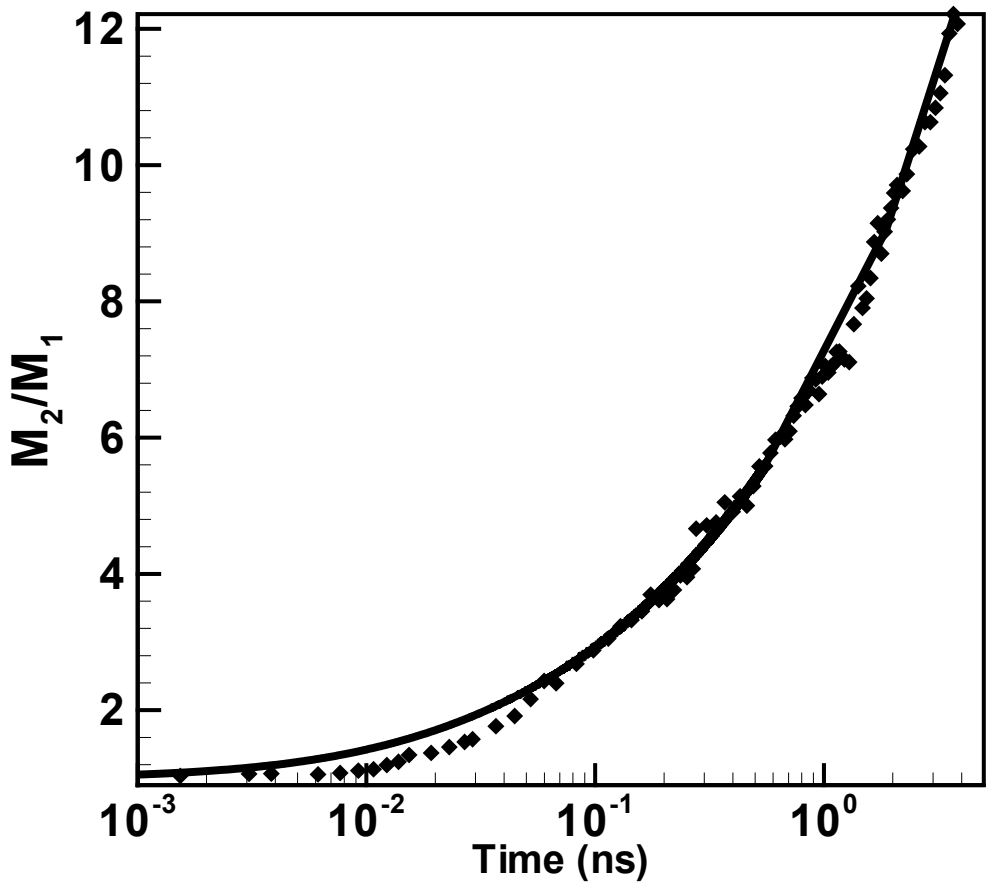

FIG. 15: Prasad and Sinno